Deep residual learning for acoustic emission source localization in A steel-concrete composite slab

Zhou, Yubao; Liang, Minfei; Yue, Xinling

Important note
To cite this publication, please use the final published version (if applicable).
Please check the document version above.

Deep residual learning for acoustic emission source localization in A steel-concrete composite slab

Yubao Zhou [a], Minfei Liang [a,*], Xinling Yue [b]

[a] *Faculty of Civil Engineering and Geosciences, Delft University of Technology, 2628CN Delft, the Netherlands*
[b] *Department of Microelectronics, Delft University of Technology, 2628CD Delft, the Netherlands*

ARTICLE INFO

ABSTRACT

Large errors can be introduced in traditional acoustic emission (AE) source localization methods using extracted signal features such as arrival time difference. This issue is obvious in the case of irregular structural geometries, complex composite structure types or presence of cracks in wave travel paths. In this study, based on a novel deep learning algorithm called deep residual network (DRN), a structural health monitoring (SHM) strategy is proposed for AE source localization through classifying and recognizing the AE signals generated in different sub-regions of critical areas in structures. Hammer hits and pencil-leak break (PLB) tests were carried out on a steel-concrete composite slab specimen to register time-domain AE signals under multiple structural damage conditions. The obtained time-domain AE signals were then converted into time-frequency images as inputs for the proposed DRN architecture using the continuous wavelet transform (CWT). The DRNs were trained, validated and tested by AE signals generated from different source types at various damage states of the slab specimen. The proposed DRN architecture shows an effective potential for AE source localization. The results show that the DRN models pre-trained by the AE signals obtained in the undamaged specimen are able to accurately classify and identify the locations of different types of AE sources with 3–4.5 *cm* intervals even when multiple cracks with widths up to 4–6 *mm* are present in the wave travel paths. Moreover, the influence factors on the model performance are investigated, including structural damage conditions, sensor-to-source distances and AE sensor mounting positions; in accordance with the parametric analyses, recommendations are proposed for the engineering application of the proposed SHM strategy.

1. Introduction

Acoustic emission (AE) technique is one of the most advanced non-destructive testing (NDT) methods for detecting internal damage sources in structures. Physically, AE refers to the transient elastic waves (also referred to as stress waves [1]) induced by a rapid release of strain energy due to deterioration process or internal friction in a solid material [2,3]. Transient elastic waves can be captured by AE sensors mounted on the surfaces of a structure by transforming them into electric signals that are then recorded by an acquisition system. Due to the passive nature of AE technique (without the need of active interrogation of the inspected structure by imposing some types of energy), it has advantages in early cracking detection and real-time monitoring. AE techniques are mainly utilized for classifying the types of damage sources [4] and estimating the locations of damage sources [5]. The scope of this study is restricted to the later.

An accurate estimation of the damage source locations is a prerequisite for further analyzing the possible cracking areas in structures and for a better insight into the characteristics of the damage sources [6]. Traditionally, two classes of AE source localization approaches can be distinguished, namely the methods based on the analysis of full AE waveforms and those considering the extracted features/parameters of recorded signals [7]. The most used AE source localization methods are the arrival-time based approaches (also referred to as travel-time-difference approaches [8]). In concrete structures, the accuracy of AE sources localization is affected by many factors, such as the picking error of signal arrival time [9] and heterogeneous material properties of concrete [10]. These factors can lead to large localization errors up to 150 *mm* in concrete structures [10]. Many advanced algorithms have been proposed to improve the AE localization accuracy, which can be classified into three categories: 1) Akaike information criterion (AIC)-based approaches for picked arrival time [11]; 2)

complex velocity model-based approaches for materials with heterogeneous properties [12,13]; and 3) the probability-based source location approaches [14]. However, these advanced algorithms often lead to longer computational time which is not suitable for real-time monitoring, and the source localization error cannot be entirely removed.

Recently, machine learning (ML) methods have been widely applied to the field of AE source localization. Compared to the aforementioned traditional source localization approaches, the data-driven ML methods are suitable for solving some difficult issues, such as the source localization in complex structures with irregular geometries. Generally, the ML-based AE source localization methods can be distinguished into two categories, the regression models and classification models [15]. The ML regression models, e.g., artificial neural network (ANN) [16,17], generalized regression [18] and random forest regressions [19], are able to predict the locations of AE sources by establishing the relationship between the training and output datasets to reproduce data's inherent characteristics [6]. These ML regression models have proven their advantages in compensation for acoustic anisotropy effects, wave reflections at structural boundaries and wave attenuation caused by defects or obstacles in wave travel paths [6,15,20,21]. Nevertheless, a large number of datasets are required for their training process, which is not practical for engineering applications [22]. Alternatively, the ML classification models achieve the prediction for AE source locations through dividing a target monitoring area into several sub-regions, in which different AE sources can be classified and recognized. The feasibility of various ML classification models for AE source localization has been widely investigated in literature, including the support vector machine (SVM) [15], hierarchical clustering algorithm [23], K-nearest neighbor (KNN) [24], naive Bayesian classifier [25] and decision trees [26]. Compared to the regression models, the number of data required for training a classification model is reduced to some extents [27].

More recently, the image-based ML classification methods have emerged as a promising tool for the AE source localization due to their potential for rapid inspection [27]. Compared with other ML-based approaches, the most distinguished advantage of an image-based ML classification method is that it does not require collecting many AE signals as inputs. A large number of datasets can be synthetically generated through the so-called "data augmentation" technique by adding a different levels of zero-mean Gaussian noise to the images [27]. The image-classification based strategy has been applied in different types of structures by adopting the convolutional neural network (CNN) based deep learning algorithms [15,28–32]. In such methods, AE signals were transformed into 2-D images or 1-D spectrograms as inputs of the CNNs [22]. The AE source locations were then predicted through classifying and recognizing the images or spectrograms corresponding to the AE signals generated in different sub-regions of a target monitoring area. The available reported literatures were still in the theoretic stage, mainly focusing on the classification of the source locations far away from each other, e.g., 100-*mm* location intervals in [27], in small-scale structures.

Although different ML models have been extensively employed for AE source localization, the previous studies usually split a single dataset, composed of same type of artificial AE sources, into different proportions of sub-datasets for the training, validation and testing of their adopted ML models [15,22,27]. AE signals of various sources types with different propagation and attenuation characteristics were observed in concrete structures [33,34]. For engineering applications, there is a need to verify the ability of ML models trained by one or several source types to predict the locations of different source types. Moreover, the previous studies mainly focused on the source localization in small-scale intact specimens in a laboratory without considering the influence of structure damage conditions on the localization accuracy. In actual working conditions, the generation of AE signals is usually accompanied by the occurrence of cracks in wave travel paths. There is a need to assess the localization accuracy of ML models trained by datasets obtained at undamaged structural state for other datasets obtained with changed (damaged) wave travel paths under multiple structural damage conditions in large-scale structures.

This paper presents an image-based deep learning framework for the AE source localization in a large-scale steel-concrete composite slab based on a novel deep learning algorithm called deep residual network (DRN). Since proposed by Microsoft Research in 2015 [35], the DRN has proven its accuracy and efficiency in image classifications; nevertheless, it has not yet been applied to the field of damage source localization. The obtained raw AE signals were converted into time-frequency images as the inputs of the proposed DRN architecture by using the continuous wavelet transform (CWT). In order to better evaluate the feasibility of the proposed strategy, in this study, the testing datasets of the established DRN models are largely different from the training datasets. The testing datasets are composed of various source types of AE signals generated under multiple damage states of the slab specimen. Moreover, the influence factors on the model performance have been investigated, including the damage conditions of the specimen (i.e., the cracks in the wave travel paths), the sensor-to-source distances and the AE sensor mounting positions (on the surfaces of steel or concrete). According to the results, recommendations were proposed for the application of the image-based AE source localization strategy to engineering practice.

2. Experimental procedure and data collection

2.1. Description of the tested specimen

A large-scale steel-concrete composite slab specimen with dimensions of $6620 \times 1794 \times 460$ mm^3 was selected for the laboratory experiments. The slab specimen was extracted from a historical bridge located in Amsterdam, The Netherlands. This slab specimen is composed of three paralleled I-shaped steel girders and the surrounding concrete parts. Four-point bending test was conducted on the slab specimen, which is part of a large experimental program for assessing the bearing capacity of historical bridge decks in The Netherlands. Fig. 1 shows the setup for the failure test, including the tested slab specimen, supports and actuators. The slab specimen was simply supported by three support cells at each side with a span of 5900 *mm*. Loads were applied through four loading plates of 230×230 mm^2 with two distributed steel beams being placed between the loading plates and two actuators.

Loading history of the test is given in Fig. 2. The load was applied for two loading-unloading cycles. In the loading of the first cycle, a loading step of 100 or 200 *kN* was adopted and crack checking was conducted at the end of each loading step. The slab was monotonically loaded to failure in the second cycle. Herein, three damage states are defined: undamaged state before loading, damaged state A at the end of the first unloading and damaged state B at the end of second unloading (Fig. 2). The cracking behavior of the slab specimen at damaged states A and B is shown in Fig. 3, providing cracking patterns at the middle part of the slab in lateral and bottom sides. The maximum widths of bottom cracks at damaged state A and B are 4 *mm* and 6 *mm*, respectively. At damaged state B, concrete crushing occurred in the top of the specimen near the loading plates (Fig. 3b).

2.2. Experimental setup and sensor layout

The AE measuring zone was selected at the bottom side of the middle part of the slab specimen, as shown in Fig. 1. In order to examine the influence of sensor-to-source distance on the model performance, a total of eight AE sensors of two different types were used in the experiments. An overview of the sensor layout is given in Fig. 4. Two R15α sensors (S1 and S2 in Fig. 4), with a resonance frequency of 150 *kHz* and a 50–400 *kHz* operating frequency range, were mounted at the bottom surface of the middle steel girder with a distance of 1.5 *m*. Six R6I-AST sensors (S3-S8 in Fig. 4), with a resonance frequency of 55 *kHz* and a 40–100 *kHz* operating frequency range, were mounted at the bottom surface of the
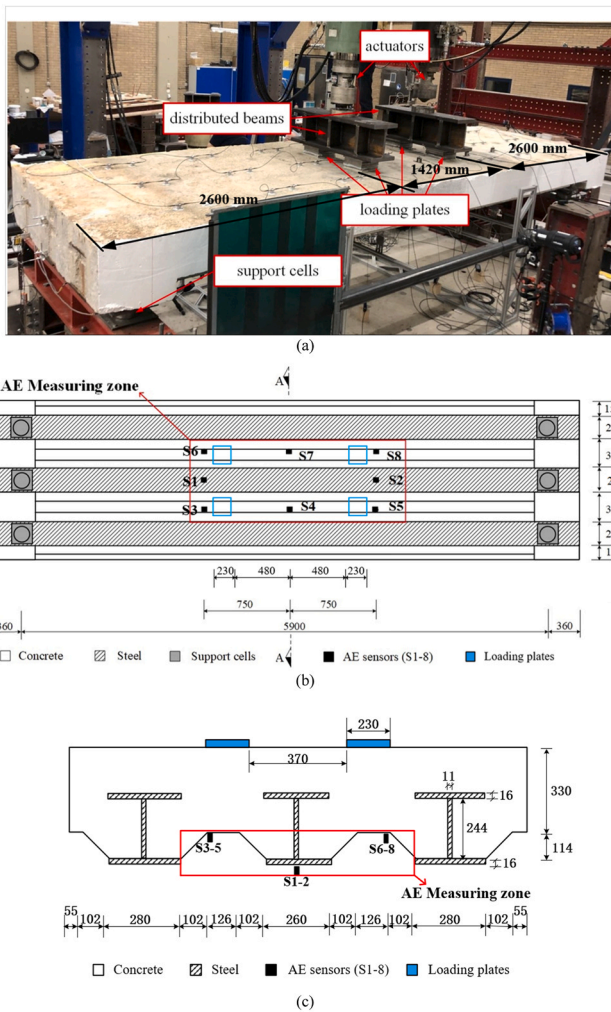
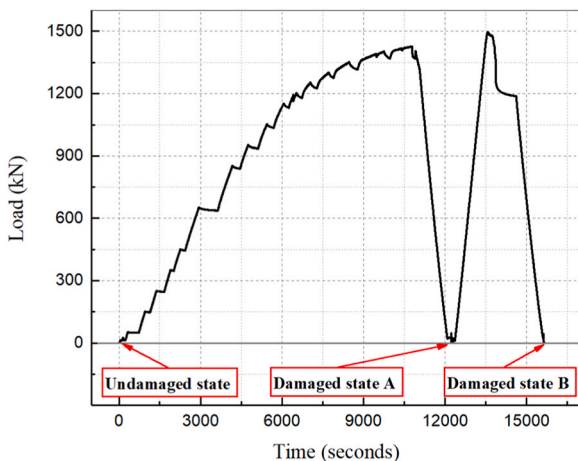Fig. 1. Description of slab specimen: (a) an overview; (b) bottom view; (c) cross section A-A (unit: *mm*).

Fig. 2. Loading history for the failure test of the slab specimen.

bottom surface of the slab specimen are marked in Fig. 1b and c.

Acquisition of AE signals was conducted using a 32-channel Micro-II Express Digital AE system (Mistras Group, Inc). A constant threshold of 45 dB was applied to isolate ambient noises (amplitudes of ambient noises were measured as around 42 dB in pretests). The pre-amplifier, pre-trigger and sampling rate were initialized as 40 dB, 256 *μs* and 5 *MHz*, respectively. A band pass filter from 20 *kHz* to 400 *kHz* was applied for all the sensors, as it is the expected frequency range for most of the detected AE signals in concrete [38] and steel structures [6]. The hit lockout time (HLT) of sensors S1 and S2 (on the steel girder surface) and the remaining sensors (on the concrete surface) were set as 1000 *μs* and 300 *μs*, respectively, to avoid false detection due to signal decay [33,39]. Silicone grease coupling agent was used and pencil-leak break tests were conducted at a 3-*cm* distance to sensor center for each sensor before main tests to assure sensor sensitivity and the proper settings of AE monitoring system.

2.3. Test procedure and data collection

This study focuses on a zone-based identification of AE source locations, as a supplement to traditional arrival-time based source localization methods. Previous study showed that classical arrival-time based AE localization approaches, e. g., the grid search method [37], can introduce large errors up to 9 cm in undamaged concrete structures [10]. Larger AE localization errors are expected when cracks in the wave travel paths and complex steel-concrete composite structures are involved as the case in this study, due to the reflection of the AE waves at the crack faces and the steel-concrete interfaces. The AE source zone is selected at the left bottom corner of the AE measuring zone with varied sensor-to-source distances from 176 to 1635 *mm* (at the bottom of slab specimen between the AE sensors S1 and S3 as shown in Fig. 5). The length of the AE source zone is set to the common error range caused by the classical arrival-time based AE localization methods for undamaged concrete structures, namely 9 cm. Eight AE source location classes are considered in the AE source zone, denoted as C1, C2, … and C8. These AE source locations are assigned on the bottom surfaces of both concrete (C1-C5) and steel (C6- C8) to represent different possible damage locations in a steel-concrete composite structure. Various distances between the AE sources, e.g., 4.5 *cm* between C1 and C2, and 3 *cm* between C4 and C5, are assigned to evaluate the localization precision of the proposed deep learning network. The DRN models were trained based on the AE signals obtained at locations C1, C2, … and C8 at the undamaged structural state. To further examine the predictivity of the DRN models for unseen datasets and entirely new datasets, two other source location classes C3T (near C3) and C6T (near C6), as marked in Fig. 5, are selected to generate additional datasets for model testing.

Artificial AE signal sources were generated at the assigned AE source locations. To increase the diversity of datasets and to be closer to real structural damage sources, four kinds of methods were used for generating AE sources, including hits from 5-mm, 10-mm and 25-mm-diameter hammers and excitations from pencil-leak break (PLB) tests, as shown in Fig. 6. Typical signals generated at source location C1 and received by AE sensor S3 (closest sensor to AE source locations as shown in Fig. 5) by the four different source generation methods are given in Fig. 7. A typical PLB signal has a peak frequency of 100 *kHz* and a wide frequency range from 20 to 120 *kHz*. The AE signals induced by the hammer hits with three different hammer diameters have a similar peak frequency at around 30 *kHz*, while those from the 25-mm diameter hammer hits cover a wider frequency range (Fig. 7c). It should be noted the frequencies and amplitudes of the signals received by different AE sensors are varied for a given excitation, due to the different sensor-to-source distances.

A total of 14 datasets were collected, as listed in Table 1, consisting of 8 main datasets and 6 additional test datasets. AE signals in the 8 main datasets were obtained by hammers of three different diameters hitting for 1000 times at AE source locations C1, …, C8, respectively, at the

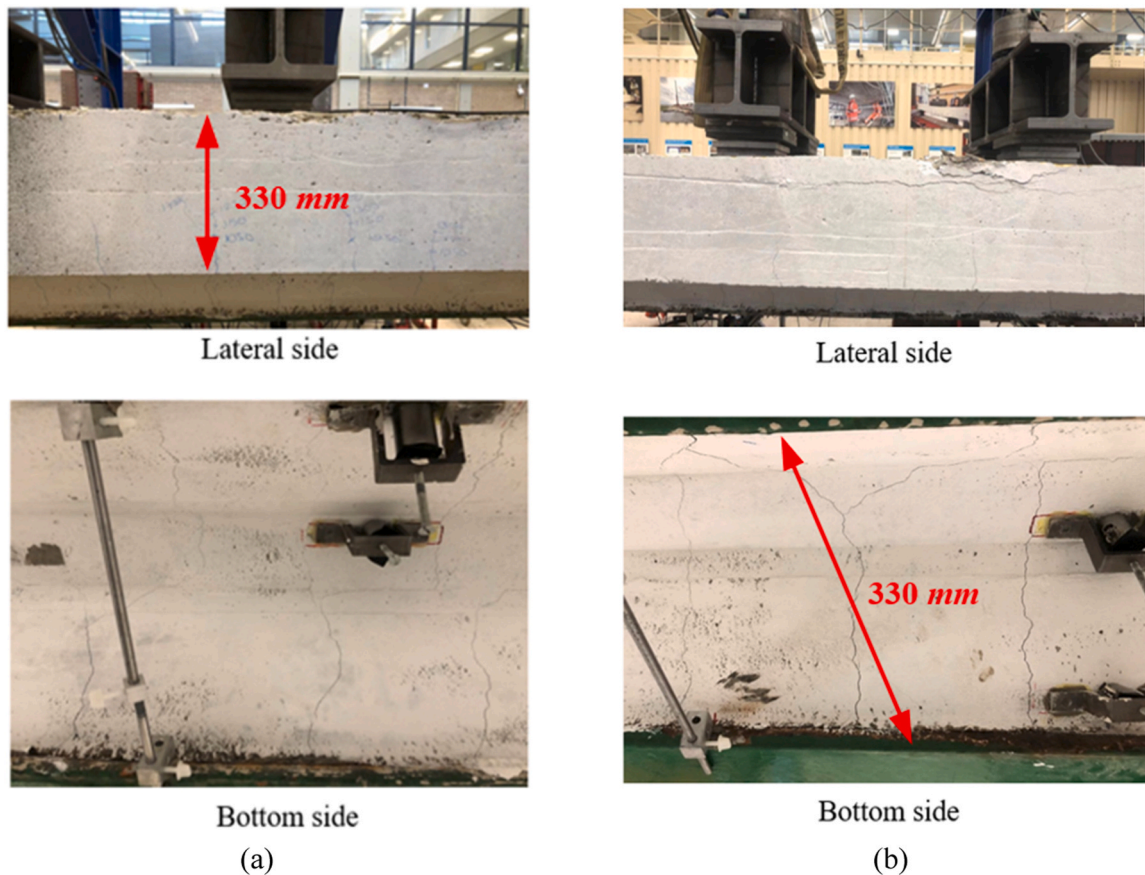concrete. Such selection of sensor types is according to the recommendation in [37] and based on different wave attenuation characteristics in concrete and steel materials. Heavier wave attenuation and lower frequency range are expected for the detected AE signals in concrete due to its heterogeneity. The precise coordinates of each AE sensor on the

Fig. 3. Cracking behavior of the slab specimen at: (a) damaged states A and (b) damaged state B.
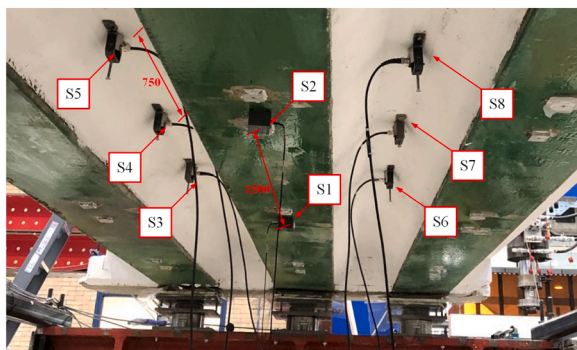

Fig. 4. An overview for AE sensor layout (unit: *mm*).

undamaged state of the slab specimen. These 8 main datasets were used for the training, validation and testing of the proposed model. AE signals in the 6 additional test datasets were generated by excitations at AE source locations C1, C8, C3T and C6T in multiple structural damage states (undamaged state, damaged states A and B) of the slab specimen. Unlike the main datasets that were generated by hammer hits, PLB sources were used for the additional test datasets. Such consideration is to preliminarily examine the feasibility of the proposed method for the localization of real damage sources. Possibility of PLB tests for simulating the acoustic emission signals from different types of real damage sources in concrete, steel and composite structures have been widely demonstrated in literature [40–42]. The PLB sources were not considered in the additional test datasets C3T, C1a and C1b, because the PLB induced signals generated at source location C3T and C1 on concrete surface cannot be detected by the remote AE sensors S5, S7 and S8 in

preliminary experiments, especially at damaged states A and B, due to their low energy and high attenuation.

Each of the AE events induced by hammer hits or PLB tests were recorded by the 8 assigned AE sensors (see Fig. 4). It should be mentioned that one excitation (hammer hits or PLB) would result in several AE signals received by an AE sensor due to the reflection of AE waves at the structural boundaries and steel-concrete interfaces. It's possible to isolate these reflection related signals by using some well-established AE signal filters, e. g., Swansong II filter [43]. However, such reflection related signals are encountered in the real working condition of a structure and thus all the received raw AE signals were retained as model inputs, in order to examine the feasibility of proposed strategy for compensating the wave reflections.

3. SHM strategy for deep residual learning based AE source localization

3.1. Data processing

The received raw AE signals are time-history data. Preliminary study showed that the proposed RDN architecture yielded low training and testing performance when the time-domain AE signals were directly used as model inputs. Similar low performance was also observed for one-dimensional CNN using time-domain ultrasonic guided wave signals as inputs [22]. Consequently, the continuous wavelet transform (CWT) was adopted to convert the raw time-series AE signals into time-frequency scalogram images that contain the time-varying frequency characteristics of received AE signals. In definition, the CWT is a convolution of the time-series signals with a set of functions generated by a wave-like oscillation (also referred to as the mother wavelet) [44]. The CWT is one of most efficient tools for image compression [45] and
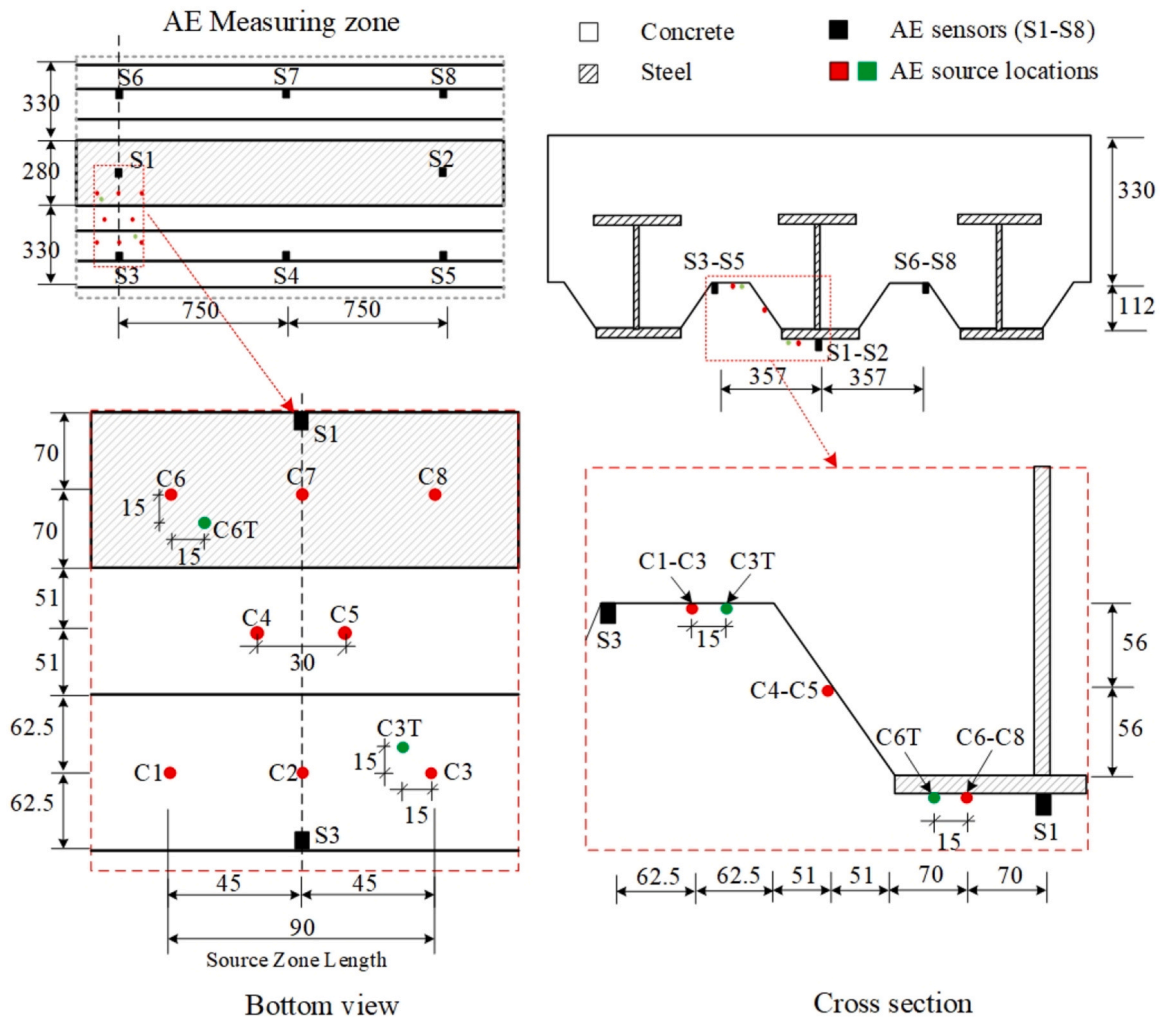
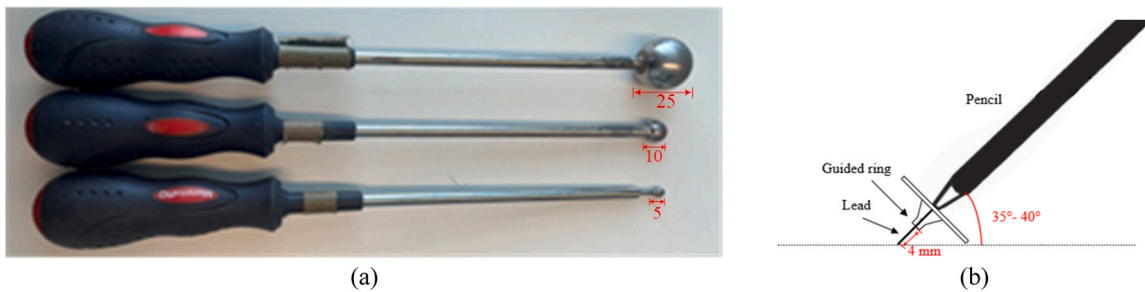**Fig. 5.** Layout of AE source locations (unit: *mm*).

Fig. 6. Different methods for generating AE sources (a) hammers and (b) pencil lead break (PLB) (unit: mm).

has the suitability for extracting features from time-series signals, such as ultrasonic guided waves and AE signals [46,47]. Each original image converted from a raw AE signal has a size of [840 × 630 × 3] (length × width × channel numbers), which was further resized to [200 × 200 × 3] for computational efficiency. To make the input space smoother and easier and to avoid overfitting and mapping problem for the input datasets, standard image augmentation was carried out through adding zero-mean Gaussian noise with 0.3 standard deviation to each resized image [48]. Accordingly, a total of 77976 images were created, with around 10000 images for each AE sensor corresponding to 9600 excitations (hammer hits or PLB sources) as shown in Table 1. The number of images (AE signals) is larger than that of the excitations, as all

the received AE signals were considered, including the reflected signals. Fig. 8 shows typical processed images from AE signals generated by a 5-mm hammer hitting at source location C1 and received by different AE sensors (S1-S8).

3.2. Brief introduction to deep residual network (DRN)

The deep residual network (DRN) is a new type of convolutional neural network (CNN). In the following, a brief introduction to the classical CNN architecture is given first. The CNN is a popular network in the computer vision field and it is usually used to construct deep learning models for the classification and identification of various ob-
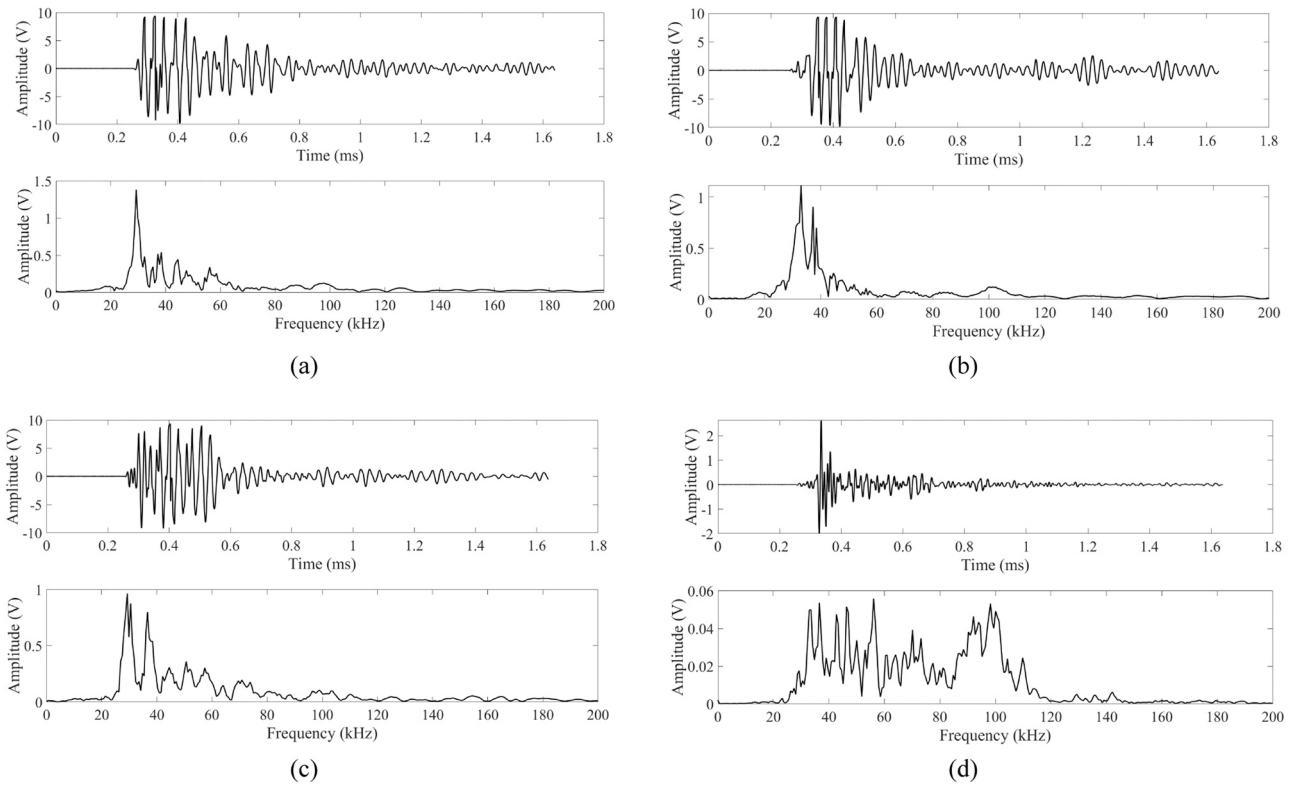
Fig. 7. Typical signals generated at source location C1 and received at AE sensor S3 by: (a) 5-mm diameter hammer hit, (b) 10-mm diameter hammer hit, (c) 25-mm diameter hammer hit and (d) pencil lead break (PLB).

Table 1
Description and classification for the collected AE signal datasets.

Dataset name	Source position	Damage state	Excitation number	Source type (percentage)	Description	Purpose (percentage)
C1	C1	undamaged	1000	5-mm diameter hammer hits (33%)	main	training (80%)
C2	C2	undamaged	1000	10-mm diameter hammer hits (33%)	datasets	validation (10%)
C3	C3	undamaged	1000	25-mm diameter hammer hits (34%)		testing (10%)
C4	C4	undamaged	1000			
C5	C5	undamaged	1000			
C6	C6	undamaged	1000			
C7	C7	undamaged	1000			
C8	C8	undamaged	1000			
C3T	C3T	undamaged	200	5-mm diameter hammer hits (33%)	additional testing datasets	testing (100%)
C1a	C1	A	200	10-mm diameter hammer hits (33%)		
C1b	C1	B	200	25-mm diameter hammer hits (34%)		
C6T	C6T	undamaged	200	PLBs (100%)		
C8a	C8	A	200			
C8b	C8	B	200			

jects, mainly images or videos [49]. A typical CNN is made up of the following building layers:

- *Input layer.* This is the first layer of a CNN, which contains the input images of three dimensions, namely the height, width and channel (s). For the colorful images used in this study, the channel number is three, i.e., red, green and blue colors.
- *Convolution layer.* In this layer, the input images are convolved to generate feature maps by using one or several filters. The filters are $m \times m$ matrixes, with m being usually set as 3, 5 or 7. Generally, several convolution layers are used in a typical CNN. In each convolution layer, the input matrix is reduced into smaller spatial size without losing any features. Element-wise multiplication operation is carried in the convolution layers involving a sliding movement of the filter [50]. Size of the sliding is given by the stride. A convolution layer can be described by the following equation:

$$F_j^{l+1} = \sum_i W_{ij}^l F_j^l + b_j^l \tag{1}$$

where F_j^l is the j-th feature map of the l-th layer. W_{ij}^l and b_j^l are the filters (also referred to as convolutional kernel [51]) and the bias, respectively, which are automatically learned by the back-propagation algorithm.

- *Activation layer.* The output values from the convolution layer are checked in this layer. Once an output value exceeds its given threshold, the activation function will be activated. The active layer is also referred to as the nonlinear mapping layer, because it works through nonlinear mapping, as follows:

$$F_j^{l+1} = f(F_j^l) \tag{2}$$

where $f(\bullet)$ represents the nonlinear activation function, such as tanh,
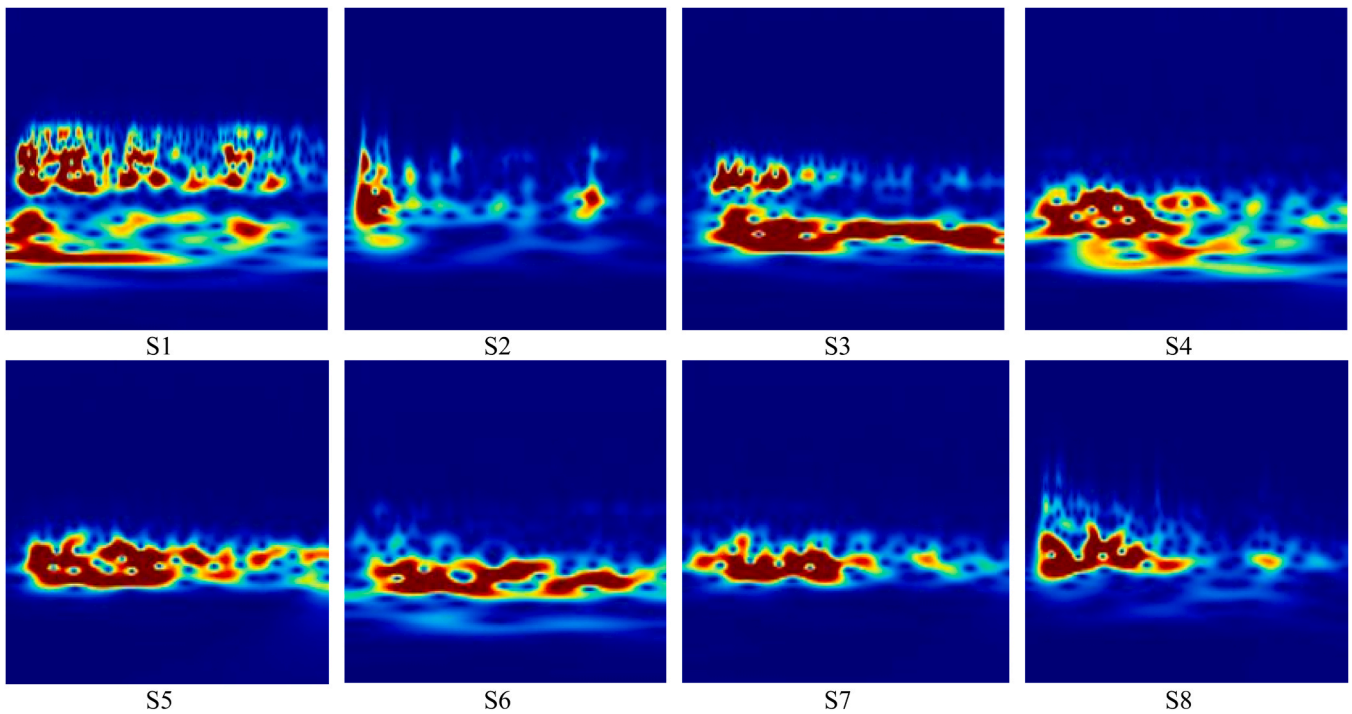
Fig. 8. Typical signals generated by a 5-mm diameter hammer hit at source location C1 received by different sensors S1-S8.

sigmoid, rectified linear unit (ReLU) and leaky ReLU [51]. One of the most used activation functions is the ReLU, which gives an output of x if x is positive else zero [52]:

$$f(x) = \begin{cases} x & x \geq 0 \\ 0 & x < 0 \end{cases} \tag{3}$$

- *Pooling layer.* This layer has a similar function with the convolution layer, namely for reducing the spatial size of input maps and compacting the extracted features. There are two types of pooling layers, including max pooling and average pooling. The max pooling and average pooling select the maximum value and the average value of a local region, respectively, as outputs.
- *Batch normalization layer.* The batch normalization layer is an optional layer. It is used to enforce the data far away from the saturation regions and thus can speed up the convergence of the CNN. A CNN with batch normalization layer is less sensitive to the initial values of parameters and thus can converge faster. Each data element x_i in a training batch β is normalized into y_i by the batch normalization layer:

$$y_i = \gamma \widehat{x_i} + \beta \tag{4}$$

where γ and β are the normalization parameters. $\widehat{x_i}$ is expressed as:

$$\widehat{x_i} = \frac{x_i - E_\beta(x_i)}{\sqrt{V_\beta(x_i)}} \tag{5}$$

where $E_\beta(x_i)$ and $V_\beta(x_i)$ are the mean and the variation of x_i in training batch β.

- *Classification layers.* The classification layers are the ending layers of a CNN, which contain the flattened layer, fully connected layer and softmax layer. The softmax function is a neural transfer function used to calculate the output of a layer from its net input. The input data will be first flattened into a single vector by the flattened layer. Each element in the flattened vector is a probability representing a certain class. The flattened vector is then transferred to the fully connected layer, where the weights and bias are applied using the activation

function. In the connected layer, a backpropagation algorithm, e.g., the stochastic gradient descent with momentum (SGDM), is implemented in each iteration of the training process. For a detailed description of CNN, readers can refer to [53–55].

The deep residual network (DRN), also referred to as deep CNN or ResNet [49], is a novel CNN type proposed by Microsoft Research in 2015 [35]. Owing to its incomparable accuracy for visual recognition tasks, the DRN have been widely applied to many deep learning systems. Compared to a classical CNN, the DRN is able to avoid vanishing gradient problem when increasing the depth of convolution layer. Although a deeper network depth can largely boost the model performance, deeper networks result in vanishing gradient problems. For the classical CNN, the gradient may be updated repeatedly until the value is very small with the backpropagation, thus preventing the change of network weight and even terminating the training process. The DRN successfully solved this problem by incorporating a residual learning method and it also show advantages in accelerating the training process [35].

As shown in Fig. 9, the DRN and traditional CNN have different network architectures. In a traditional CNN, the architecture is organized through combining different basic units (layers) in a cascade manner. In a residual network, the input and output in a building block
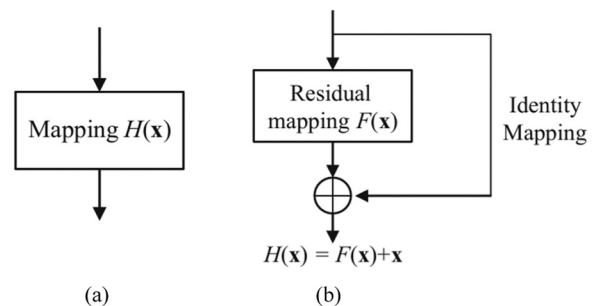

Fig. 9. Basic building blocks in: (a) a typical CNN and (b) a DRN. (adapted from [51]).

are directly connected by a shortcut pathway. Unlike the CNN architecture that directly approximates an underlying function $H(x)$, the DRN fits its residual mapping $F(x)$, as shown in Eq. (6). Fitting a residual mapping $F(x)$ is much easier than the original mapping $H(x)$, especially when $H(x)$ is an identity or near identity mapping [51]. This property makes it possible to largely increase the network depth while without decreasing the accuracy of network. For a detailed description of DRN, readers can refer to [35].

$$F(x) := H(x) - x \qquad (6)$$

3.3. Proposed network architecture

A block diagram for the DRN architecture adopted in this study is illustrated in Fig. 10. The proposed DRN architecture is built based on four kinds of blocks, including input block B1, initial convolution block B2, identity block B3 and residual convolutional block B4. The block B1 and B2 were sequentially used once at the top layers, while B3 and B4 were iteratively stacked four times in the deep layers. The B1 block is mainly used for data preprocessing to 1). normalize the image tensor using its mean and standard deviation values and then 2). add gaussian random noise with a zero mean and standard deviation of 0.3. The aim of introducing gaussian random noise here is for data augmentation to prevent overfitting. The block B2 with a 7 * 7 filter and a stride of 2 is to extract the information in a larger local area and form a down-sampled feature map to achieve higher computation accuracy. Afterwards, the blocks B3 and B4 were iteratively used in sequence to conduct residual mapping, feature extraction and down-sampling. Note that no pooling layers were used in the blocks B3 and B4 and the down-sampling was conducted by a stride of 2 in the B4 convolutional layers. Among all the blocks, each convolutional layer was followed by a batch normalization layer to ensure the numerical stability and reduce overfitting. The rectified linear unit (ReLU) function was used as the activation function to introduce nonlinearity following each batch normalization layer. At the end, the 7 * 512 feature map was passed on to an average pooling layer to further reduce the dimension of feature map and flatten it to a 1 * 8192 vector. Finally, a fully-connected forward neural network with a dropout rate of 0.4 in the hidden layer and a softmax activation function in the final layer is used to output the predicted probability

distribution of different locations.

3.4. Network training

Training of the DRN is an optimization process based on the stochastic gradient descent with momentum (SGDM), which minimizes the loss of the training dataset by updating bias and weights [27]. The loss function is calculated in each step of the optimization process, which is considered as the softmax function with multi-nominal logistic loss in this study [55]. The input vectors of the loss function include the image pixel, weight and bias. For a given feature samples X (i.e., the image pixel), parameters of the DRN (i.e., the weight and bias) are learned by minimizing the following loss function L:

$$L = -\frac{1}{N}\sum_{i=1}^{N}\sum_{k=1}^{K}\delta(y_i = k) \bullet \log\left(\frac{e^{o_{ik}(X_i,\theta)}}{\sum e^{o_{ik}(X_i,\theta)}}\right) \qquad (7)$$

where y_i is the label of the i-th sample X_i. $\delta(\bullet)$ is the delta function. N and K are the total numbers of training samples and labels, respectively. $o_{ik}(X_i,\theta)$ denotes the output of the sample X_i. θ denotes the network parameters, which can be the weight matrix W or the bias vector b. The following gradient descent is used to update the weight matrix and bias vector for each layer:

$$W(t+1) = W(t) - \alpha\frac{\partial L}{\partial W} \qquad (8)$$

$$b(t+1) = b(t) - \alpha\frac{\partial L}{\partial b} \qquad (9)$$

where α is the user-defined learning rate that is selected according to information accuracy and computational time. It should be mentioned that, in Eqs. (8) and (9), all the training samples are involved in the computation of the total loss L. For a K-class classification problem, the loss function is the cross-entropy for a 1-of-K coding scheme. Accordingly, the logarithmic loss calculated from Eqs. (7–9) is also referred to as cross-entropy loss [27].
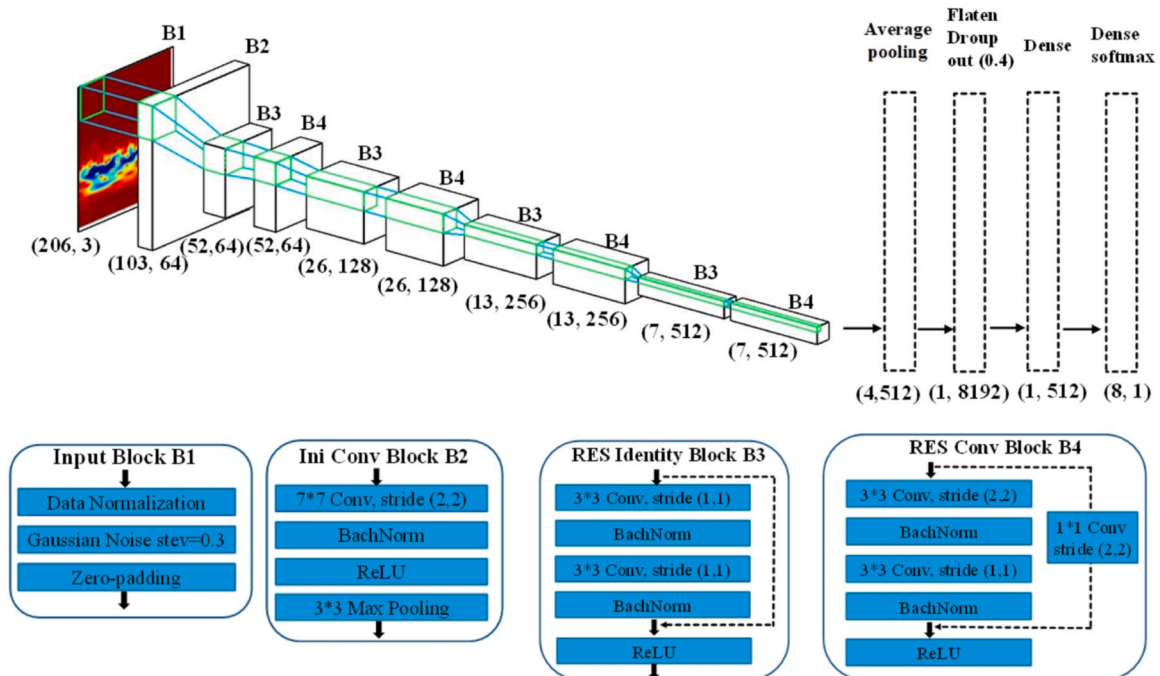

Fig. 10. Proposed DRN architecture (stev: standard deviation; Ini: initial; Conv: convolutional layer; ReLU: rectified linear unit).

4. Results

A total of eight models were established based on the proposed DRN architecture corresponding to the eight assigned AE sensors (Fig. 5) in order to investigate the influence of sensor-to-source distance on the model performance. The processed CWT images were used as inputs for training, validation and testing of the established DRN models. Herein, for simplicity, same names are used for the established DRN models and their corresponding AE sensors, e.g., DRN model S1 means that its inputs are made up of the processed CWT scalogram images converted from the AE signals received by AE sensor S1. Two classes of datasets were considered, i.e., the main datasets and additional test datasets (Table 1). Each DRN model was first trained, validated and test based on the main datasets that were hammer hits induced AE signals obtained at the un-damaged state of the slab specimen. The pre-trained models were then further tested based on the additional test datasets composed of six testing cases that consider new (neighbouring) source locations, new AE source type (PLB sources) and multiple damage states of the tested slab specimen (Table 1).

4.1. Network performance for main datasets

The main datasets of around 8000 images per AE sensor totaled 67560 samples, which were split into 80%, 10% and 10% proportions for training, validation and testing purposes, respectively. Each DRN model (Model S1, …, S8) was trained for 40 epochs with 31 iterations in each epoch without overfitting occurring. The training-validation results in terms of cross-entropy loss and accuracy curves for the DRN model S1 are given Fig. 11. The cross-entropy loss and accuracy curves of the remaining seven DRN models are shown in Appendix A. For DRN model S1, the validation accuracy converges at approximately 15–20 epochs as shown in the decreasing cross-entropy loss curve (Fig. 11a). The validation accuracy of the eight established DRN models all converge after 30 epochs (Appendix A). The confidence for accurate predictions of all DRN models are gradually improved, although several oscillations can be observed in both the validation accuracy and cross-entropy loss curves in early epochs (before convergence) due to the limited data in each batch [27]. After convergence, the eight established DRN models all achieve more than 99.5% training/validation accuracies. The test performance of DRN model S1 for the main datasets is shown in Fig. 12. Refer to Appendix A for the test performance of the remaining DRN models for the main datasets. The predictive test accuracies of DRN models S1-S8 are 99.89%, 99.78%, 99.88%, 99.50%, 100% and 99.63%, respectively. This indicates that the proposed DRN network is promising for the classifying AE locations with 3–4.5 *cm* intervals when the training and testing data are generated by same type of AE sources (hammer hits in the main dataset) in the undamaged steel-concrete composite slab specimen. Moreover, it can be concluded that the sensor-to-source distance has little influence on the predictive
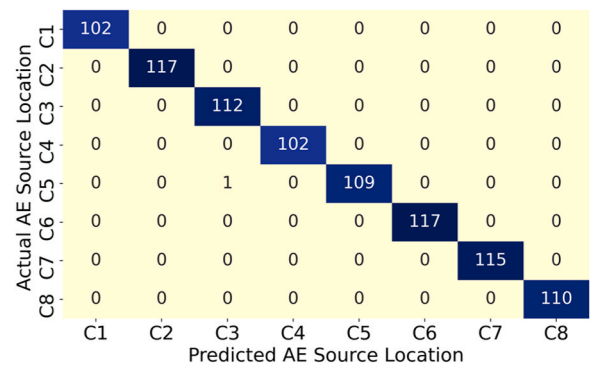

Fig. 12. Confusion matrix of the test performance of DRN model S1 for main datasets.

performance of the proposed DRN network for the main datasets, as the test accuracies of near 100% are achieved by all the DRN models corresponding to the eight assigned AE sensors with varied distances of 0.18–1.6 *m* to sources.

4.2. Network performance for additional test datasets

In actual working conditions, the received AE signals are the stress waves induced in the fracture process of materials [2]. This implies that the generation of AE signals is usually accompanied by the occurrence of cracks in wave travel paths. Moreover, AE signals with various peak frequencies of 0–350 *kHz* were observed for different types of damage or fracture in concrete structures [33,34]. Therefore, although the proposed DRN architecture provides accurate predictive testing results for the main datasets as discussed above, such results cannot demonstrate its potential for damage source localization in engineering practice due to the lack of data diversity and representativeness in the main datasets. As shown in Table 1, the main datasets consist of the same type of data obtained all by hammers hitting on fixed source positions (C1-C8) at the undamaged state of the slab specimen.

Consequently, the DRN models (models S1, …, S8) that had been pre-trained by the main datasets were then further tested for six additional test datasets, including the datasets C3T, C6T, C1a, C8a, C1b and C8b involving new source locations (i.e., neighbouring sources locations C3T and C6T), new AE source types (i.e., PLB sources) and multiple damage conditions of the tested slab specimen (see Table 1). The six additional test datasets of around 200 × 6 images per AE sensor totaled 10416 samples for testing purpose. During the testing process for the additional test cases, the test datasets C3T, C6T, C1a, C8a, C1b and C8b were supplied from the test dataset channels C3, C6, C1, C8, C1 and C8 of the DRN network, respectively.

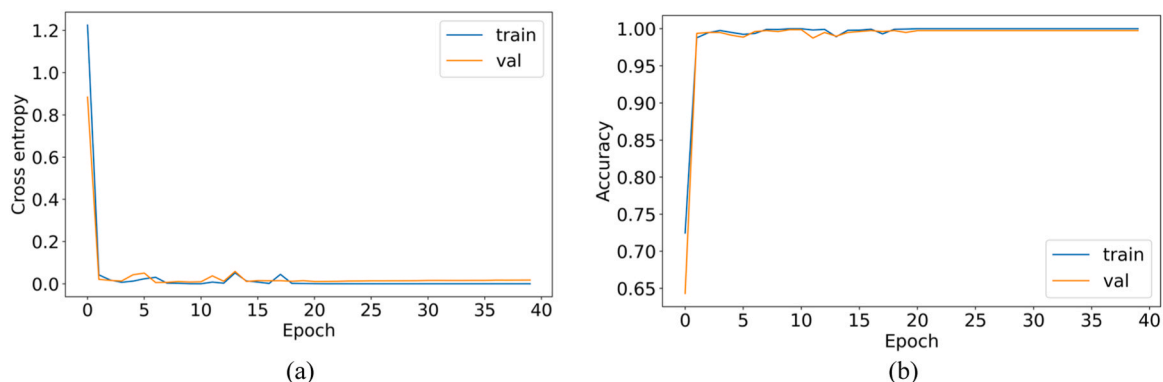Fig. 13 and Fig. 14 show the test performance of DRN models S1 and

Fig. 11. Typical training-validation results of DRN model S1: (a) cross-entropy loss and (b) accuracy.
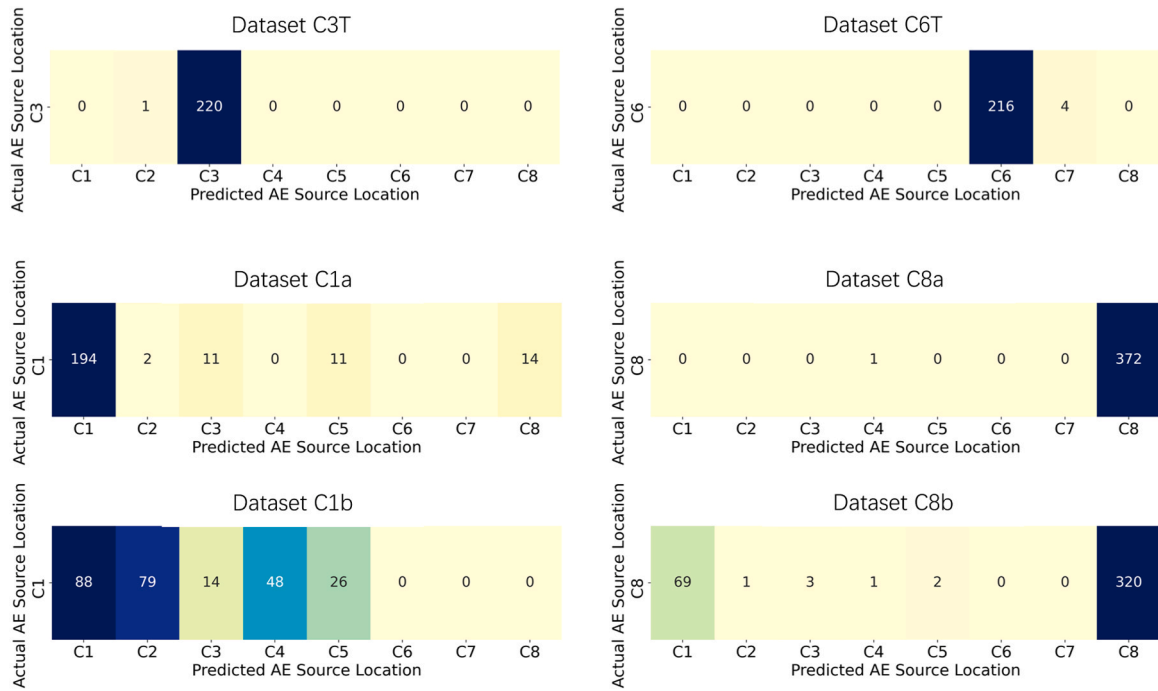
Fig. 13. Confusion matrixes of the test performance of DRN models S1 for 6 additional testing cases.
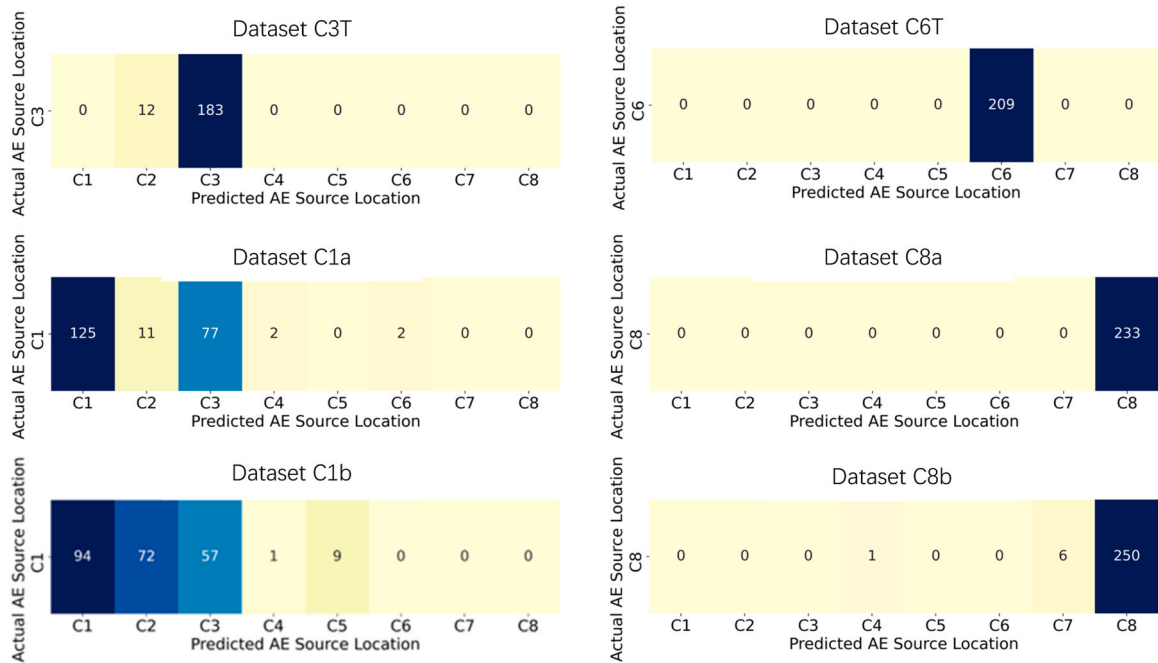

Fig. 14. Confusion matrixes of the test performance of DRN models S3 for 6 additional testing cases.

S3 (models established based on the AE signals received at AE sensors S1 and S3 with closer distances to the AE source zone as shown in Fig. 5), respectively, for the six additional test datasets. It can be observed that the proposed DRN architecture provides accurate test results for the cases involving new source locations, with the test accuracies of model S1 (S3) being 99.5% (93.8%) and 98.2% (100%) for datasets C3T and C6T, respectively.

For datasets C1a, C1b, C8a and C8b that were obtained at damaged states A and B of the slab specimen, declines of different degrees can be observed in the test accuracies of DRN models S1 and S3. For the test cases corresponding to AE source C1 located on the concrete surface (i.

e., datasets C1a and C1b), the test accuracies of models S1 and S3 are both dramatically reduced with accumulating damage in the slab specimen. The test accuracies of model S1 (S3) are 83.6% (57.6%) and 34.5% (40.3%) for datasets C1a and C1b, respectively. However, it should be noted that the misclassifications for C1a and C1b datasets by models S1 and S3 are mainly the nearby AE source locations C2 and C3 with close distances of 4.5–9 *cm* to the target source location C1 (see Fig. 5). This implies the proposed DRN network still remains the predictive ability for AE source classification, although its classification precision declines with increasing crack widths in wave travel paths.

For the datasets C8a and C8b corresponding to AE source location C8

located on steel surface, the damage states of the slab specimen show little influence on the test accuracy of DRN models S1 and S3. The test accuracies of DRN model S1 (S3) are 99.7% (100%) and 80.8% (97.3%) for datasets C8a and C8b, respectively. This can be explained by the different damage conditions in the steel and concrete parts of the slab specimen. At damage states A and B, large surface cracks of 4–6 *mm* widths occurred in the concrete parts while no visible damage was observed in the steel parts, as shown in Fig. 3. In such cases, the wave travel paths of AE signals generated on the concrete surface (datasets C1a and C1b) were largely changed, while AE signals generated on the steel surface (datasets C8a and C8b) can still travel through the almost undamaged steel girders. As a result, less differences may be existed between the AE signals in the additional test datasets C8a and C8b and those in the training dataset C8.

Unlike the main datasets with accurate test results independent from the distance between AE sensors and sources, the sensor-to-source distance has a large influence on the predictive test accuracy of the proposed DRN architecture for the additional testing cases. The test performances of all the DRN models for the 6 additional test datasets are given in Appendix B. For a clear discussion, the test accuracies of eight DRN models for the additional test cases are further summarized in Table 2. The predictive test accuracies of the proposed DRN network exhibit a declined tendency for the six additional test datasets with increasing the sensor-to-source distances. When the sensor-to-source distances are larger than 770 mm, accuracies of the proposed DRN architecture are reduced to less than 60% for most test cases. Due to wave attenuation, the signals received at remote AE sensors would contain less useful information in both time and frequency domains. Additionally, a longer sensor-to-source distance means more cracks are involved in the wave travel paths at damaged states A and B, increasing the differences between signals in training and testing datasets, and thus leading to the classification and identification difficulty for the DRN network.

Comparing the six test datasets, the proposed DRN network gives more accurate prediction for datasets C8a and C8b corresponding to AE source location C8 located on steel surface, for which the AE sensors with 176–994 *mm* distances to sources all provide more than 73% predictive accuracies. Moreover, it should be mentioned that the predictive accuracy of the proposed DRN network is also affected by the mounting positions of AE sensors. As shown in Table 2, AE sensors S2, S5 and S8 have similar distances to the AE sources. However, the proposed DRN network achieves more accurate test performance for the signals received at sensor S2, as it is mounted on the steel surface that is less affected by the damaged states of the slab. In accordance with these results, recommendations can be proposed for the application of the DRN-based SHM strategy to engineering practice. The AE sensor should be mounted on the steel parts of a steel-concrete structure with a distance no more than 770 *mm* to the targeted AE source zone, to assure an accurate prediction of the proposed DRN network.

5. Discussion

This study proposed a practical AI-based SHM strategy for

engineering applications by combining the AI tool and traditional AE source localization methods. Although with relatively large localization errors, the traditional AE source localization approaches considering the extracted signal features such as arrival time difference or amplitude attenuation can give a rough estimate for the source locations. When more precise AE source localization is needed, a rough location zone first estimated by traditional AE methods can be selected as the targeted area for AI models. Then, the targeted area can be further divided into sub-regions of different sizes according to the needed localization precision. AE signals generated in these sub-regions can be classified and recognized by an AI-based classification model like the DRN network used in this study. This largely reduces the number of datasets and computation costs for training an accurate AI model. Moreover, in order to better evaluate the feasibility of AI models, this study performed the training, validation and testing of the DRN models using different datasets consisted of AE signals from different source types at multiple damage states of the specimen.

Some limitations of current study should be mentioned. First, although the similarity between PLB sources and real damage sources has been widely discussed and demonstrated in literatures (e.g., [40–42]), the PLB signals generated on specimen surfaces as the cases in this study and in most available literatures [14,15,56,57–60] have different propagation characteristics from the real damage sources generated inside structures (i.e., body waves). It's not able to determine the precise source locations of the AE signals from concrete cracking or delamination between concrete and steel in the failure process of the adopted slab specimen. Therefore, the localization accuracy of the DRN models for the real cracking sources cannot be quantified using the AE data obtained in this study. To thoroughly verify the feasibility and accuracy of data-driven AI models for the localization of real damage sources, special experimental programs with known damage source locations (e.g., those in [33,34,61] with controlled or localized damage areas in specimens) should be adopted to obtain real damage signals that can be labelled for model testing. Nevertheless, the predictive ability of the proposed DRN-based SHM strategy should not be denied, as significant differences still exist in the hammer hits and PLB induced signals used for training and testing purposes, respectively. The hammer hits induced signals have relatively narrowed frequency ranges at around 30 *kHz*, while a typical PLB induced signal shows a wider frequency range of 20–120 *kHz* (Fig. 7).

Secondly, the manual signal generation method used in current study (i.e., the hammer hit) is laborious and time-consuming and thus not suitable for creating a large training dataset in practice. In future study, the automatic source generator [22] can be an alternative which is also able to generate signals with different central frequencies. In fact, different frequency bands in a AE signal show largely different wave propagation and attenuation characteristics [62]. The proposed DRN architecture achieves its predictive ability by extracting the time-varying frequency characteristics of AE signals (see Section 3.1). If signals of various frequencies could be included in the training datasets, the predictive ability of the DRN model would be enhanced by learning the wave propagation and attenuation characteristics of different frequency bands.

Table 2
Test accuracies of the eight DRN models for six additional testing cases.

Sensor number	Sensor mounting position	Distance to source zone (mm)	Test accuracies for additional datasets (%)					
			Dataset C3T	Dataset C6T	Dataset C1a	Dataset C1b	Dataset C8a	Dataset C8b
S3	concrete	176	93.8	100	53.5	40.3	100	97.3
S1	steel	191	99.5	98.2	83.6	34.5	99.7	80.8
S6	concrete	653	82.1	60.3	48.5	14.4	86.5	72.8
S4	concrete	770	82.7	53.8	36.6	18.8	80.1	84.9
S7	concrete	994	54.9	33.5	20.7	9.3	73.4	78.6
S5	concrete	1510	49.3	0	0	0	0	0
S2	steel	1512	51	35.5	41.1	23.8	77.9	88.8
S8	concrete	1635	37.3	0	33.8	33.4	0	2.3

6. Conclusions

Based on a novel deep learning algorithm called deep residual network (DRN), this study proposes a zone-base AE source localization strategy through classifying and recognizing the AE signals generated in different sub-regions of a critical area. The proposed strategy has proven its potential for AE source localization at multiple damage states of a structure, representing a big step towards developing a practical artificial intelligence-based method for locating real damage sources in in-service structures. The main results are as follows:

1. Feasibility and accuracy of the proposed AE source localization strategy have been demonstrated. For the datasets obtained at the undamaged state of the slab specimen, the pre-trained DRN can effectively distinguish the 8-class source locations with 3–4.5 cm intervals. Eight pre-trained DRN models, corresponding to 8 AE sensors with varied distances of 0.18–1.6 m to sources, exhibit test accuracies of 99.89%, 99.78%, 99.88%, 99.50%, 100% and 99.63%, respectively, for the main dataset.
2. The predictive ability of the proposed AE source localization strategy has been preliminarily proved. The DRN pre-trained by hammer hits induced signals in the undamaged slab specimen can effectively classify and recognize the source locations of pencil lead break (PLB) induced signals at multiple damaged states of the specimen. The pre-trained DRN models S1 and S3, corresponding to two AE sensors with less than 0.2 m distances to sources, exhibit 100% (97.3%) and 99.7% (80.8%) test accuracies, respectively, for the PLB signals at damaged state A (B).
3. Influence factors on the localization precision of the proposed approach have been investigated. When large cracks of 4–6 mm widths occurring in the slab specimen at damage states A and B, the localization precision of the DRN models decreases. In addition, accuracy of the DRN is largely reduced with increasing the sensor-to-

source distances. A sensor-to-source distance of no more than 0.77 m is recommended to assure the predictive accuracy of the DRN. The mounting positions of AE sensors also influences the performance of the DRN. More accurate prediction is achieved by the DRN models established corresponding to the AE sensors mounted on the steel surface than those mounted on the concrete surface.

CRediT authorship contribution statement

Yue Xinling: Writing – review & editing, Visualization, Validation, Supervision, Data curation. **Liang Minfei:** Writing – review & editing, Writing – original draft, Visualization, Validation, Software, Methodology, Investigation, Formal analysis, Data curation, Conceptualization. **Zhou Yubao:** Writing – review & editing, Writing – original draft, Visualization, Validation, Software, Resources, Project administration, Methodology, Investigation, Funding acquisition, Formal analysis, Data curation, Conceptualization.

Declaration of Competing Interest

The authors declare that they have no known competing financial interests or personal relationships that could have appeared to influence the work reported in this paper.

Data availability

Data will be made available on request.

Acknowledgment

Appendix

A. *The training-validation results and testing confusion matrixes of the 8 established models (S1- S8) for the main datasets.*
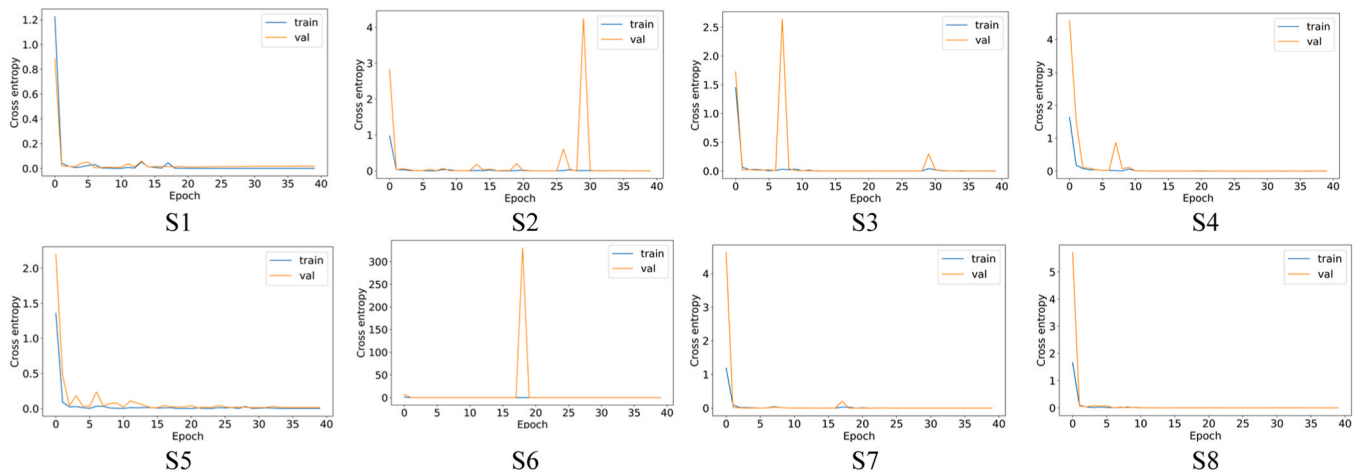

Fig. A1 Cross-entropy loss curves for the training-validation process of eight DRN models for main datasets.
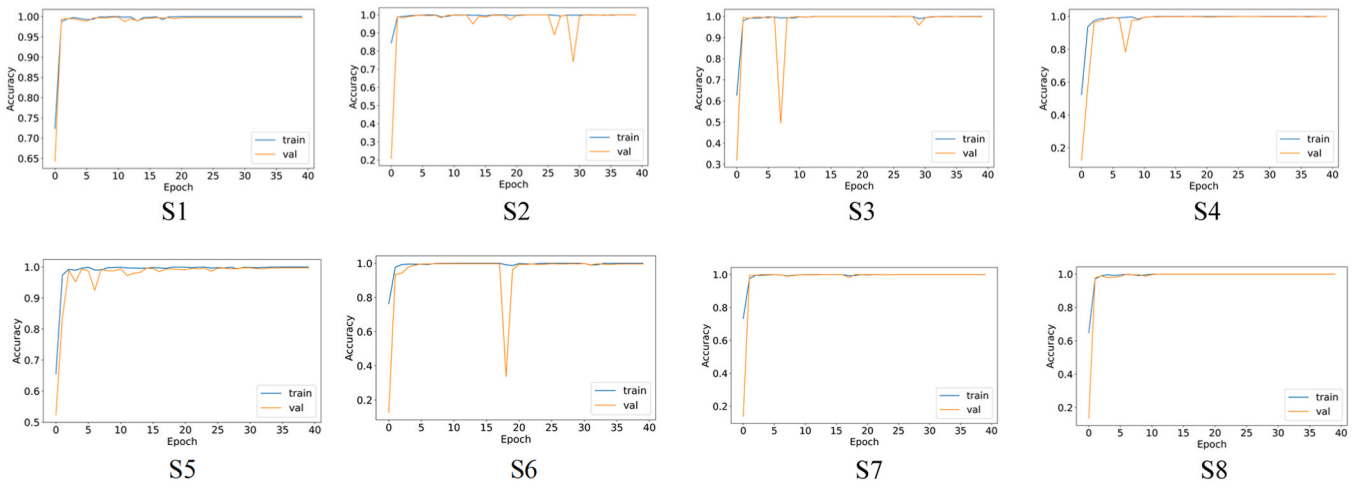
Fig. A2 Training and validation accuracy of eight DRN models for main datasets.
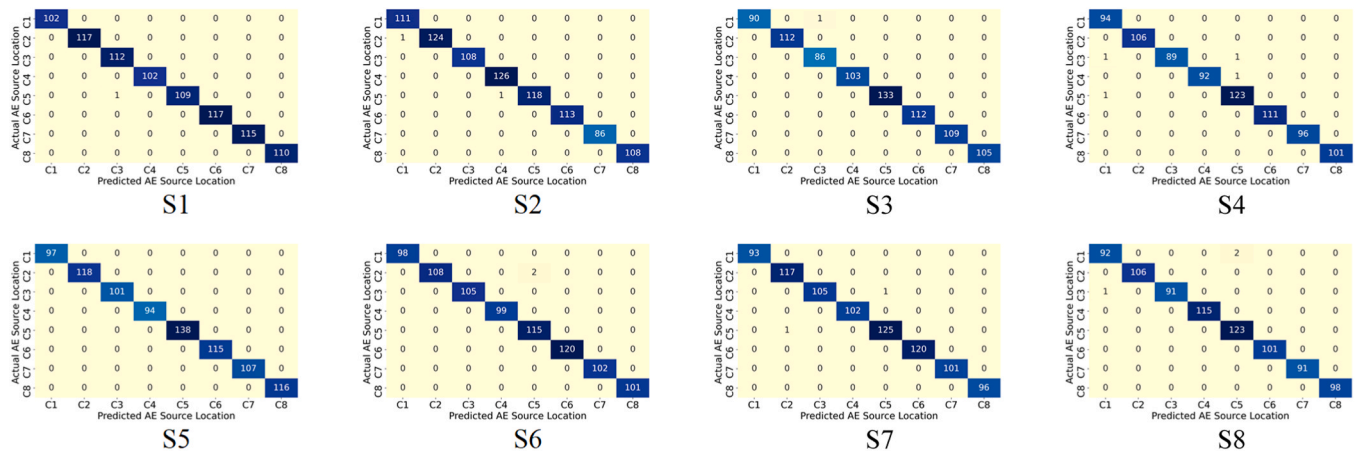

Fig. A3 Confusion matrixes of the test performance of eight DRN models for main datasets.

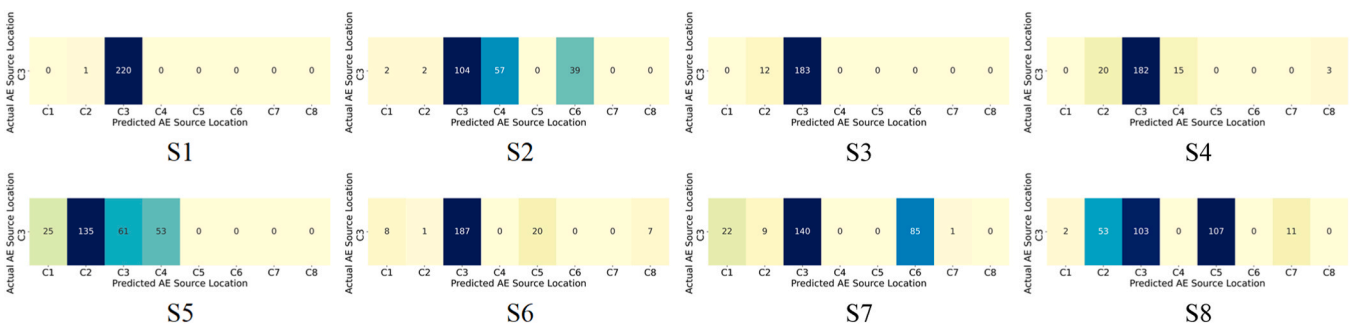B. *Confusion matrixes of the test performance of eight DRN models for six additional test datasets.*

Fig. B1. Confusion matrixes of the test performance of eight DRN models for dataset C3T.

Fig. B2. Confusion matrixes of the test performance of eight DRN models for dataset C6T.

Fig. B3. Confusion matrixes of the test performance of eight DRN models for dataset C1a.

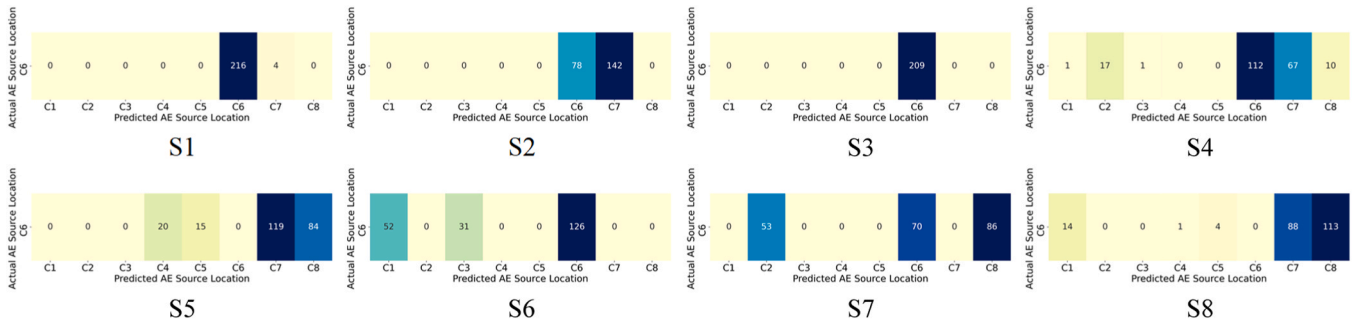**Fig. B4.** Confusion matrixes of the test performance of eight DRN models for dataset C1b.

Fig. B5. Confusion matrixes of the test performance of eight DRN models for dataset C8a.
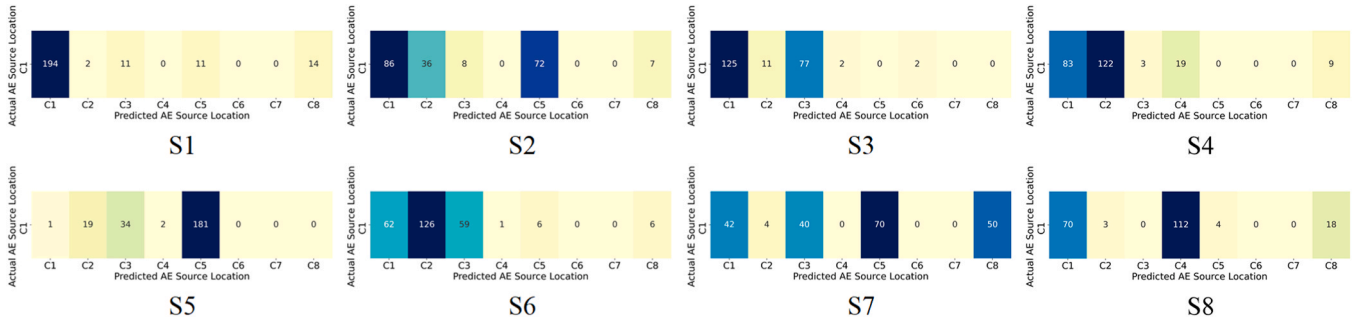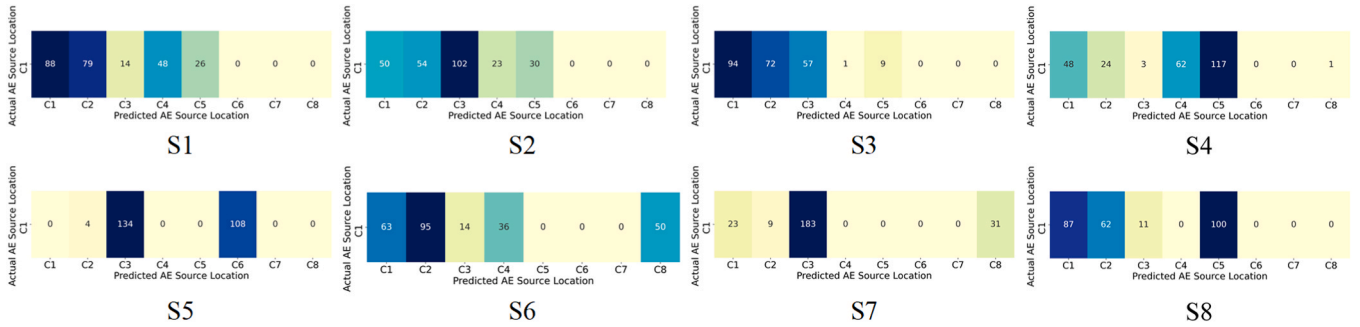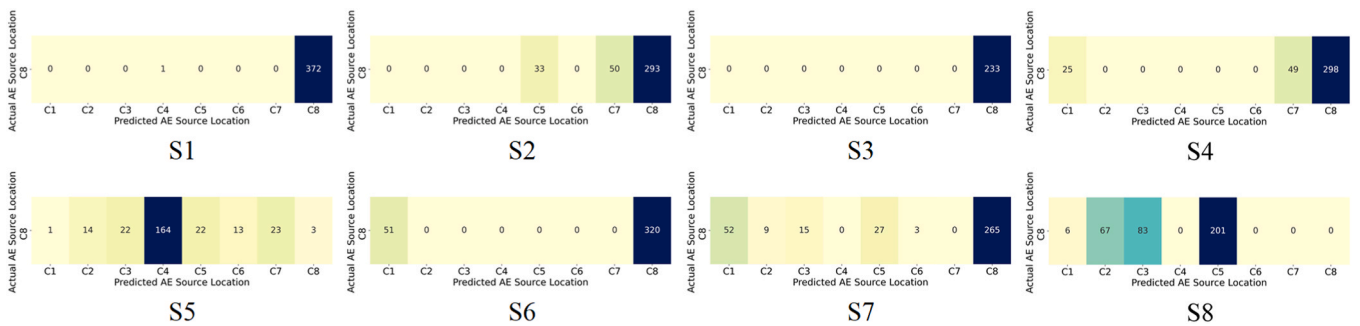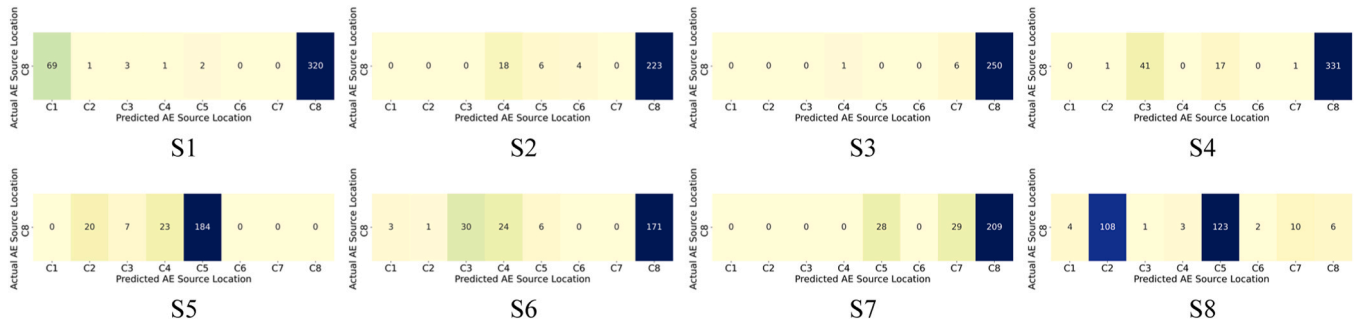
Fig. B6. Confusion matrixes of the test performance of eight DRN models for dataset C8b.

References

[1] A. Lisjak, Q. Liu, Q. Zhao, O.K. Mahabadi, G. Grasselli, Numerical simulation of acoustic emission in brittle rocks by two-dimensional finite-discrete element analysis, Geophys. J. Int. 195 (1) (2013) 423–443.

[2] I. Iturrioz, G. Lacidogna, A. Carpinteri, Experimental analysis and truss-like discrete element model simulation of concrete specimens under uniaxial compression, Eng. Fract. Mech. 110 (2013) 81–98.

[3] Zheng, Y., et al., Fractal Characteristics and Damage Evaluation of Corroded Beams Under Four-Point Bending Tests Based on Acoustic Emission Techniques. Available at SSRN 4117393.

[4] T. Pan, Y. Zheng, Y. Zhou, W. Luo, X. Xu, C. Hou, Y. Zhou, Damage pattern recognition for corroded beams strengthened by CFRP anchorage system based on acoustic emission techniques, Constr. Build. Mater. 406 (2023), 133474.

[5] T. Kundu, Acoustic source localization, Ultrasonics 54 (1) (2014) 25–38.

[6] L. Cheng, H. Xin, R.M. Groves, M. Veljkovic, Acoustic emission source location using Lamb wave propagation simulation and artificial neural network for I-shaped steel girder, Constr. Build. Mater. 273 (2021), 121706.

[7] K.M. Holford, D. Carter, Acoustic emission source location. Key Engineering Materials, Trans Tech Publ., 1999.

[8] D.J. Sypeck, H.N. Wadley, Characterization of Fiber Fracture Via Quantitative Acoustic Emission. Nondestructive Characterization of Materials VIII, Springer,, 1998, pp. 635–640.

[9] B. Schechinger, T. Vogel, Acoustic emission for monitoring a reinforced concrete beam subject to four-point-bending, Constr. Build. Mater. 21 (3) (2007) 483–490.

[10] E. Tsangouri, G. Karaiskos, A. Deraemaeker, D. Van Hemelrijck, D. Aggelis, Assessment of acoustic emission localization accuracy on damaged and healed concrete, Constr. Build. Mater. 129 (2016) 163–171.

[11] J.H. Kurz, C.U. Grosse, H.-W. Reinhardt, Strategies for reliable automatic onset time picking of acoustic emissions and of ultrasound signals in concrete, Ultrasonics 43 (7) (2005) 538–546.

[12] T. Nishida, et al., Damage evaluation of RC bridge deck under wheel loading test by means of AE tomography, Prog. Acoust. Emiss. XVIII (2016) 111–116.

[13] S. Gollob, Source localization of acoustic emissions using multi-segment paths based on a heterogeneous velocity model in structural concrete, ETH Zurich,, 2017.

[14] M.R. Jones, T.J. Rogers, K. Worden, E.J. Cross, A Bayesian methodology for localising acoustic emission sources in complex structures, Mech. Syst. Signal Process. 163 (2022), 108143.

[15] A. Jierula, S. Wang, T.M. Oh, J.W. Lee, J.H. Lee, Detection of source locations in RC columns using machine learning with acoustic emission data, Eng. Struct. 246 (2021) 112992.

[16] V. Soltangharaei, R. Anay, L. Assi, M. Bayat, J.R. Rose, P. Ziehl, Analyzing acoustic emission data to identify cracking modes in cement paste using an artificial neural network, Constr. Build. Mater. 267 (2021) 121047.

[17] S. Farhangdoust, et al., Prediction of damage location in composite plates using artificial neural network modeling. Sensors and Smart Structures Technologies for Civil, Mechanical, and Aerospace Systems 2019, SPIE,, 2019.

[18] M.A. Pillai, et al., Acoustic source localization using random forest regressor. 2019 International Symposium on Ocean Technology (SYMPOL), IEEE,, 2019.

[19] Z.H. Liu, Q.L. Peng, X. Li, C.F. He, B. Wu, Acoustic emission source localization with generalized regression neural network based on time difference mapping method, Exp. Mech. 60 (5) (2020) 679–694.

[20] A. De Fenza, A. Sorrentino, P. Vitiello, Application of artificial neural networks and probability ellipse methods for damage detection using lamb waves, Compos. Struct. 133 (2015) 390–403.

[21] S. Kalafat, M.G. Sause, Acoustic emission source localization by artificial neural networks, Struct. Health Monit. 14 (6) (2015) 633–647.

[22] G. Azuara, M. Ruiz, E. Barrera, Damage localization in composite plates using wavelet transform and 2-d convolutional neural networks, Sensors 21 (17) (2021) 5825.

[23] S.K. Al-Jumaili, M.R. Pearson, K.M. Holford, M.J. Eaton, R. Pullin, Acoustic emission source location in complex structures using full automatic delta T mapping technique, Mech. Syst. Signal Process. 72 (2016) 513–524.

[24] T.B. Quy, S. Muhammad, J.-M. Kim, A reliable acoustic EMISSION based technique for the detection of a small leak in a pipeline system, Energies 12 (8) (2019) 1472.

[25] T. Boczar, S. Borucki, D. Jancarczyk, M. Bernas, P. Kurtasz, Application of selected machine learning techniques for identification of basic classes of partial discharges occurring in paper-oil insulation measured by acoustic emission technique, Energies 15 (14) (2022) 5013.

[26] N. Morizet, N. Godin, J. Tang, E. Maillet, M. Fregonese, B. Normand, Classification of acoustic emission signals using wavelets and random forests: application to localized corrosion, Mech. Syst. Signal Process. 70 (2016) 1026–1037.

[27] S. Sikdar, D. Liu, A. Kundu, Acoustic emission data based deep learning approach for classification and detection of damage-sources in a composite panel, Compos. Part B: Eng. 228 (2022), 109450.

[28] Simonyan, K. and A. Zisserman, Very deep convolutional networks for large-scale image recognition. arXiv preprint arXiv:1409.1556, 2014.

[29] Krizhevsky, A., I. Sutskever, and G. Hinton, ImageNet classification with deep convolutional neural networks. Advances in Neural Informa-tion Processing System 25 (NIPS 2012). *2012*. 2017.

[30] V. Ewald, R.M. Groves, R. Benedictus, DeepSHM: A deep learning approach for structural health monitoring based on guided Lamb wave technique. Sensors and Smart Structures Technologies for Civil, Mechanical, and Aerospace Systems 2019, SPIE,, 2019.

[31] S. Zhang, C.M. Li, W. Ye, Damage localization in plate-like structures using time-varying feature and one-dimensional convolutional neural network, Mech. Syst. Signal Process. 147 (2021), 107107.

[32] C. Su, M. Jiang, S. Lv, S. Lu, L. Zhang, F. Zhang, Q. Sui, Improved damage localization and quantification of CFRP using Lamb waves and convolution neural network, IEEE Sens. J. 19 (14) (2019) 5784–5791.

[33] Y. Zheng, Y. Zhou, Y. Zhou, T. Pan, L. Sun, D. Liu, Localized corrosion induced damage monitoring of large-scale RC piles using acoustic emission technique in the marine environment, Constr. Build. Mater. 243 (2020) 118270.

[34] Zhou, Y., Y. Zhou, and Y. Zheng. AE Monitoring Corrosion-induced Deterioration of Reinforced Concrete Piles in The Simulated Marine Environment. in IOP Conference Series: Earth and Environmental Science. 2019. IOP Publishing.

[35] He, K., et al. Deep residual learning for image recognition. in Proceedings of the IEEE conference on computer vision and pattern recognition. 2016.

[37] C.U. Grosse, M. Ohtsu, Acoustic emission testing, Springer Science & Business Media,, 2008.

[38] M. Ohtsu, The history and development of acoustic emission in concrete engineering, Mag. Concr. Res. 48 (177) (1996) 321–330.

[39] Y. Zheng, Y. Zhou, Y. Zhou, T. Pan, Q. Zhang, D. Liu, Cracking behavior of reinforced concrete beams strengthened with CFRP anchorage system under cyclic and monotonic loading, Eng. Struct. 207 (2020), 110222.

[40] Falcetelli, F., et al. Modelling of pencil-lead break acoustic emission sources using the time reversal technique. in Proceedings of the 9th European Workshop on Structural Health Monitoring, Manchester, UK. 2018.

[41] Sause, M.G., Investigation of pencil-lead breaks as acoustic emission sources. 2011.

[42] Lopes, B.G., et al. Study on the effect of the temperature in Acoustic Emission Sensor by the Pencil Lead Break Test. In 2018 13th IEEE International Conference on Industry Applications (INDUSCON). 2018. Ieee.

[43] A.A. Abouhussien, A.A. Hassan, Application of acoustic emission monitoring for assessment of bond performance of corroded reinforced concrete beams, Struct. Health Monit. 16 (6) (2017) 732–744.

[44] X. Tang, Q. Li, Time-frequency analysis and wavelet transform, Science Press,, Beijing, China, 2008.

[45] W.C. Lang, K. Forinash, Time-frequency analysis with the continuous wavelet transform, Am. J. Phys. 66 (9) (1998) 794–797.

[46] S. Legendre, D. Massicotte, J. Goyette, T.K. Bose, Wavelet-transform-based method of analysis for Lamb-wave ultrasonic NDE signals, IEEE Trans. Instrum. Meas. 49 (3) (2000) 524–530.

[47] A. Migot, Y. Bhuiyan, V. Giurgiutiu, Impact localization on composite plates using two developed imaging methods. Active and Passive Smart Structures and Integrated Systems XIV, SPIE,, 2020.

[48] X. Ying, An overview of overfitting and its solutions, J. Phys.: Conf. Ser. (2019) (IOP Publishing).

[49] J.S. Chou, M.A. Karundeng, D.N. Truong, M.Y. Cheng, Identifying deflections of reinforced concrete beams under seismic loads by bio-inspired optimization of deep residual learning. Struct. Control Health Monit. 29 (4) (2022), e2918.

[50] J. Gu, S. Liu, Z. Zhou, S.R. Chalov, Q. Zhuang, A stacking ensemble learning model for monthly rainfall prediction in the Taihu Basin, China, Water 14 (3) (2022) 492.

[51] S. Wu, S. Zhong, Y. Liu, Deep residual learning for image steganalysis, Multimed. tools Appl. 77 (9) (2018) 10437–10453.

[52] Glorot, X., A. Bordes, and Y. Bengio. Deep sparse rectifier neural networks. in Proceedings of the fourteenth international conference on artificial intelligence and statistics. 2011. JMLR Workshop and Conference Proceedings.

[53] L. Minfei, G. Yidong, C. Ze, W. Zhi, S. Erik, Š. Branko, Microstructure-informed deep convolutional neural network for predicting short-term creep modulus of cement paste, Cem. Concr. Res. 152 (2022), 106681.

[54] Y. Zhou, Y. Zheng, Y. Liu, T. Pan, Y. Zhou, A hybrid methodology for structure damage detection uniting FEM and 1D-CNNs: demonstration on typical high-pile wharf, Mech. Syst. Signal Process. 168 (2022), 108738.

[55] O'Shea, K. and R. Nash, An introduction to convolutional neural networks. arXiv preprint arXiv:1511.08458, 2015.

[56] N. Ince, C.S. Kao, M. Kaveh, A. Tewfik, J. Labuz, A machine learning approach for locating acoustic emission, EURASIP J. Adv. Signal Process. 2010 (2010) 1–14.

[57] Q. Zhao, S.D. Glaser, Relocating acoustic emission in rocks with unknown velocity structure with machine learning, Rock. Mech. Rock. Eng. 53 (5) (2020) 2053–2061.

[58] N.K. Banjara, S. Sasmal, S. Voggu, Machine learning supported acoustic emission technique for leakage detection in pipelines, Int. J. Press. Vessels Pip. 188 (2020), 104243.

[59] P. Karvelis, G. Georgoulas, V. Kappatos, C. Stylios, Deep machine learning for structural health monitoring on ship hulls using acoustic emission method, Ships Offshore Struct. 16 (4) (2021) 440–448.

[60] A. Ebrahimkhanlou, S. Salamone, Single-sensor acoustic emission source localization in plate-like structures using deep learning, Aerospace 5 (2) (2018) 50.

[61] T. Pan, Y. Zheng, Y. Zhou, Y. Liu, K. Yu, Y. Zhou, Coupled effects of corrosion damage and sustained loading on the flexural behavior of RC beams strengthened with CFRP anchorage system, Compos. Struct. 289 (2022), 115416.

[62] Pan, T., et al. Damage Mode Identification of CFRP-Strengthened Beam Based on Acoustic Emission Technique. in International Symposium of the International Federation for Structural Concrete. 2023. Springer.